Full length article

The role of Ti and TiC nanoprecipitates in radiation resistant austenitic steel: A nanoscale study

Niels Cautaerts [a,b,*], Rémi Delville [a], Erich Stergar [a], Janne Pakarinen [c], Marc Verwerft [a], Yong Yang [d], Christina Hofer [e], Ronald Schnitzer [e], Steffen Lamm [f], Peter Felfer [f], Dominique Schryvers [b]

[a] *Fuel Materials Group, Institute for Nuclear Materials Science, SCK•CEN, Boeretang 200, Mol BE-2400, Belgium*

[b] *EMAT, Department of Physics, University of Antwerp, Groenenborgerlaan 171, Antwerp BE-2020, Belgium*

[c] *Studsvik Nuclear AB, Atomvägen 1, Tystberga 610 60, Sweden*

[d] *Materials Science and Engineering Department, University of Florida, 100 Rhines Hall, Gainesville, FL 32611, USA*

[e] *Department of Materials Science, Montanuniversität Leoben, Franz Josef-Straße 18, Leoben 8700, Austria*

[f] *Department of Materials Science and Engineering, Friedrich-Alexander-Universität Erlangen-Nürnberg, Martensstraße 5, Erlangen 91058, Germany*

ARTICLE INFO

ABSTRACT

This work encompasses an in-depth transmission electron microscopy and atom probe tomography study of Ti-stabilized austenitic steel irradiated with Fe-ions. The focus is on radiation induced segregation and precipitation, and in particular on how Ti and TiC affect these processes. A 15-15Ti steel (grade: DIN 1.4970) in two thermo-mechanical states (cold-worked and aged) was irradiated at different temperatures up to a dose of 40 dpa. At low irradiation temperatures, the cold-worked and aged materials evolved to a similar microstructure dominated by small Si and Ni clusters, corresponding to segregation to small point defect clusters. TiC precipitates, initially present in the aged material, were found to be unstable under these irradiation conditions. Elevated irradiation temperatures resulted in the nucleation of nanometer sized Cr enriched TiC precipitates surrounded by Si and Ni enriched shells. In addition, nanometer sized Ti- and Mn-enriched G-phase ($M_6Ni_{16}Si_7$) precipitates formed, often attached to TiC precipitates. Post irradiation, larger number densities of TiC were observed in the cold-worked material compared to the aged material. This was correlated with a lower volume fraction of G-phase. The findings suggest that at elevated irradiation temperatures, the precipitate-matrix interface is an important point defect sink and contributes to the improved radiation resistance of this material. The study is a first of its kind on stabilized steel and demonstrates the significance of the small Ti addition to the evolution of the microstructure under irradiation.

© 2020

1. Introduction

Austenitic stainless steels play a very important role as structural materials for nuclear reactor internals. This can be attributed to their excellent mechanical properties at elevated temperature and well established fabrication technology. In most next generation liquid metal cooled reactors under development, such as the MYRRHA reactor at SCK-CEN in Belgium [1], the fuel will be contained in cladding tubes made from austenitic steel.

The main drawback of using austenitic steels as cladding is that these materials are prone to so called volumetric swelling [2]: when exposed to a fast neutron flux at intermediate to elevated temperatures (300–700 °C) for extended periods of time, the material experiences a near isotropic volumetric expansion. The microscopic origin of this phenomenon is the growth of nanometer sized cavities due to clustering of vacancies [3,4]. Vacancies become supersaturated in the material due to the atomic displacements induced by irradiation, which is a driving force for void nucleation. The voids tend to grow because there is a preferential absorption and annihilation of the opposite defects (self-interstitial atoms or SIA) on dislocations, leading to a net flux of vacancies to the voids [5]. Since neutron fluxes and temperatures are the most extreme in the cores of reactors, swelling of the cladding material is one of the biggest challenges hindering the deployment of liquid metal cooled reactors. Hence, already since the late 1960′s and early 1970′s, there has been a huge effort in the US [6], France [7–9], Russia [10,11], Japan [12–14] and India [15] to improve the swelling resistance of austenitic alloys by appropriate alloying and thermo-mechanical processing.

Swelling in austenitic steels starts with an incubation stage with limited swelling, which precedes a steady state stage where 1%

swelling per displacements per atom or dpa (a unit of irradiation dose) is observed [16]. Steady state swelling is similar for a wide range of microstructures and alloy compositions, whereas the incubation stage is very sensitive to these parameters [17–21]. Therefore, the efforts to improve swelling behavior are mostly focused on extending the incubation stage by optimizing the alloying and thermo-mechanical history. Cold-worked Ti stabilized steels with high Ni content, specifically the 15-15Ti grades (15 wt% Cr, 15 wt% Ni), show significantly longer incubation times than solution annealed steels or non-stabilized variants such as 316 alloys (18 wt% Cr, 10 wt% Ni) [2,22]. Ti additions are thought to decrease vacancy mobility and hence inhibit their clustering, since Ti is an oversized solute in austenite which binds preferentially to vacancies [20]. In addition, due to the high affinity of Ti for C, TiC nucleates as nano-sized MC precipitates on lattice defects such as dislocations [23]. By trapping or annihilating point defects at their interface, these small precipitates could also contribute to an improved swelling resistance.

However, the role of these small precipitates in the microstructural development under irradiation is not well understood, and as a result their importance is debated [10]. The transition from the incubation stage to the steady state stage is often correlated with so called "microstructural instability", indicated by the formation of various radiation induced phases and the subsequent depletion of certain alloying elements in the matrix [10,24–26]. In all austenitic steels, Ni and Si tend to segregate to sinks due to radiation induced segregation (RIS) [27–31] and can form phases such as G-phase ($M_6Ni_{16}Si_7$ with M = Mn, Ti, Cr,...) and γ' (Ni_3Si)[32]. Many detailed microstructural studies on these phases have been performed in irradiated 304 and 316 steels [27,29,33,34] but not in Ti stabilized steels. A better understanding of the improved swelling resistance could be obtained by investigating the interaction between Ti, TiC and the radiation induced phases. This may in turn lead to new alloy improvement strategies.

In addition, there is uncertainty about the irradiation temperature window in which the nanoprecipitates are stable. Some authors reported their redissolution at low irradiation temperatures ($< 300\ °C$) [35] while others suggested the opposite [14]. In the past, these materials have been irradiated mostly at temperatures relevant to sodium cooled reactors (450-600 °C) [2,7,36], where TiC nanoprecipitates are known to nucleate during irradiation. The low temperature regime (300-450 °C) is less investigated, but still of particular interest to lead-bismuth cooled reactor systems for which operating temperatures are limited by corrosion [37].

Hence, the goal of this study was two-fold: to better understand the stability of TiC nanoprecipitates under irradiation and to elucidate how their presence influences irradiation induced precipitation. In this pursuit, 15-15Ti steel was irradiated with heavy ions in order to test multiple irradiation conditions and arrive at a mechanistic understanding. To investigate the effect of pre-irradiation microstructure, both thermally aged steel (which contained nanoprecipitates) and cold-worked steel (which did not) were irradiated. After irradiation, the microstructures were quantitatively studied using atom probe tomography (APT) and transmission electron microscopy (TEM).

2. Materials and methods

The material used in this study was titanium stabilized austenitic steel with nuclear fuel cladding as intended application [38]. The overall composition provided by the manufacturer SANDVIK is given in Table 1. The as-received material was in the form of thin walled tubes with an outer diameter of 6.55 mm and a wall thickness of 450 μm. The material was subjected to a solution heat treatment between 1100 and 1140 °C for 4 minutes before being cold-drawn to 24% cross-sectional area reduction. The as-received material is referred to as the cold-worked or c.w. state. Material in the aged state was produced by heat treating the c.w. material for 2 hours at 800 °C in air.

Table 1

Chemical composition and measurement uncertainties of DIN 1.4970 cladding tubes as given by the manufacturer SANDVIK. Concentrations were measured by X-ray fluorescence (XRF) unless another technique is indicated in brackets.

Element	wt. %	at. %
C (HFIR) [a]	0.10 ± 0.01	0.46 ± 0.05
Cr	15.08 ± 0.08	16.04 ± 0.09
Ni	15.04 ± 0.15	14.17 ± 0.14
Mn	1.83 ± 0.03	1.84 ± 0.03
Mo	1.21 ± 0.01	0.698 ± 0.006
Ti	0.49 ± 0.02	0.57 ± 0.02
Si	0.56 ± 0.06	1.1 ± 0.1
B (ICP-MS) [b]	0.0028 ± 0.0005	0.014 ± 0.003
P	0.013 ± 0.001	0.023 ± 0.002
N (EXTR) [c]	0.011 ± 0.001	0.043 ± 0.004
V	0.034 ± 0.005	0.037 ± 0.005
Cu	0.026 ± 0.001	0.023 ± 0.001
Co	0.020 ± 0.002	0.019 ± 0.002
Fe	Bal.	Bal.

[a] Combustion technique, see ASTM E1019 [39].
[b] Inductively coupled plasma mass spectrometry.
[c] Combustion technique, see ASTM E1019 [39].

The characterization of the c.w. and aged materials was published elsewhere [40,41], but a summary is given here. The c.w. material contains no MC nanoprecipitates but does contain many large primary (Ti,Mo)C and Ti(N, C) precipitates; the former present as particles in the 0.05-1 μm range and the latter as particles in the 1–10 μm range. Due to the presence of these phases, the austenite matrix only contains 0.28 ± 0.01 at% Ti and 0.18 ± 0.01 at% C. The dislocations have a cell type structure with cells between 50–200 nm in diameter. Some grains are heavily twinned. The aged material contains a fine distribution of (Ti,Mo,Cr)C nanoprecipitates on dislocations with a number density of $(4 \pm 1) \times 10^{22}$ m^{-3}-3 and an average diameter of 3.7 ± 0.2 nm; their composition is approximately 40 at% Ti, 10 at% Cr, 10 at% Mo, and 40 at% C. Large precipitates of (Ti,Mo)C and $M_{23}C_6$ are also present on grain boundaries and incoherent twin segments. Compared to the c.w. material, the Ti and C contents in the matrix are reduced to 0.10 ± 0.01 at% and 0.06 ± 0.02 at% respectively.

Samples for ion irradiation were made by punching out 3 mm diameter discs that were ground to a thickness of 100–200 μm (final grit size: 2000). These were subsequently electropolished at 20-25V on one side (by taping off one of the holes in the holder) in a Struers Tenupol-3 using Struers A2 electrolyte (perchloric acid and ethanol based) cooled to between –20 and –10 °C. This drew a current of approximately 0.1 A. Samples were electropolished to about halfway the initial sample thickness to ensure the surface to be irradiated would be unaffected by artifacts introduced by grinding.

Fe-ion irradiations were performed at the Michigan Ion Beam Laboratory in Ann Arbor, USA. For each irradiation, six electropolished discs were clamped between an assembly of two steel plates with the electropolished side facing the ion beam. This assembly was mounted on a copper heating plate. Thermal contact between the samples and the backplate was ensured with a thin copper spacer. Mechanical stability of the samples was ensured with crushable tungsten washers between the samples and the top plate. The temperature at the sample surface was monitored with a thermal imaging camera calibrated with readings from thermocouples spot-welded on dummy samples. Backplate heating was adjusted to account for beam heating, to ensure the desired irradiation temperature at the sample surface. Irradiations were performed at three temperatures: 300 °C, 450 °C and 600 °C. At each condition, two discs of both the c.w. and aged material were irradiated. Throughout

this paper, the different samples are often referred to with the short-hand notation [irradiation temperature]/[aged/c.w.].

Fe^{2+} ions at 4.5 MeV were used in the form of a rastering beam with an average current of 0.4 μA or 1.2×10^{12} ions.s^{-1}. The total scan area varied somewhat between different irradiations but was around 12×12 mm^2, resulting in an average flux of 9×10^{11} ions.s^{-1}.cm^{-2}. The dose in dpa was calculated using the SRIM program [42,43] using the Kinchin and Pease (K-P) model [44] with displacement energy $E_d = 40$ eV. The calculation showed that 4.5 MeV Fe^{2+} ions yield an irradiated layer of approximately 1.5 μm; the damage profile is overlaid on some figures in the results section. The material was irradiated until an integrated dose of 40 dpa was achieved at the surface. To calculate this, the dose rate was periodically updated over the course of the irradiation based on the scan area and the beam current.

Samples for TEM observations and APT measurements were prepared using standard Focused Ion Beam (FIB) lift-out techniques. The instruments used were an FEI (ThermoFisher) Quanta (situated at CAES, Idaho falls, USA) and ThermoFisher DualBeam Scios (situated at SCK•CEN, Mol, Belgium). In order to minimize Ga-ion beam damage effects, the final thinning of the TEM lamellae and shaping of APT tips was performed with 2 kV Ga$^+$ ions.

For TEM studies a JEOL 3000F (situated at the University of Antwerp, Belgium) equipped with a Schottky FEG source operating at 300 kV was used. The microscope was also equiped with a GATAN GIF 2000 EELS spectrometer, which was used to estimate the sample thickness.

APT measurements were conducted on two CAMECA (IMAGO) LEAP-4000X HR instruments (situated at CAES, Idaho falls, USA and FAU, Erlangen, Germany) and one LEAP-3000X HR (situated at MU Leoben, Austria), all with the reflectron geometry and a detection efficiency around 37–39%. Measurements were conducted in laser mode with laser energy 40–60 pJ on the LEAP-4000X HR and between 0.3-0.6 nJ on the LEAP-3000X HR. For all measurements, the base temperature was between 40-70K, the pulse frequency was between 200–250 kHz and the evaporation rate was between 0.5-1% of the pulse frequency. All raw APT measurement files as well as the reconstructions made and used in this paper can be downloaded as a separate data archive. APT results were analyzed with IVAS 3.8.0 and 3Depict 0.0.21 [45].

Characterizations in this paper focus on the top few hundred nm (estimated <500 nm) in order to minimize the influences of the injected Fe atoms and the curvature of the dpa profile. Hence, most results presented in this paper represent microstructures irradiated to a range between 40–70 dpa, with a weighted average of 50 dpa as estimated from the SRIM profile. APT samples were prepared such that milling at 5 kV was stopped 1–2 seconds after the Pt layer was no longer visible in the back-scattered electron image. The subsequent 2 kV milling step removed 100–200 nm. Most TEM results are presented in this paper as overviews to show the entire irradiated layer. For sizing and counting the precipitates high magnification images were collected close to the irradiated surface.

Additional graphics explaining the sample preparation procedures and the ion irradiation are provided in the supplementary materials.

3. Results

3.1. Low irradiation temperature: 300 °C

After irradiation at the lowest temperature (300 °C), the irradiated layer was void of small precipitates both in the c.w. and aged condition. Fig. 1 shows a composite dark field (DF) image using the $g = (002)_{TiC}$ reflection. The calculated dose profile is overlaid on the figure. Whereas the bulk (>1.5 μm depth) contained a high number of small nanoprecipitates seen as small white dots, the irradiated layer was deprived of any TiC precipitates. This indicates that TiC was redis-
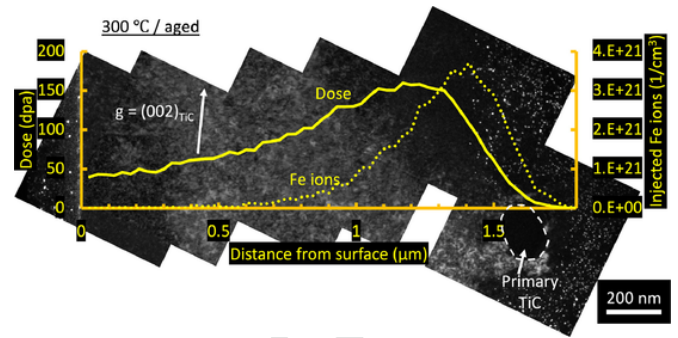

Fig. 1. The irradiated layer in the aged sample irradiated at 300 °C, imaged in dark field (DF) with $g = (200)_{TiC}$, shows a complete absence of TiC nanoprecipitates. The denuded zone corresponds well with the dose profile depth predicted by SRIM, shown in the overlay. The calculated injected interstitial concentration is also plotted. Circled with a white dotted line is a large primary TiC particle with a 200 nm diameter, located at the edge of the irradiated layer.

solved under these irradiation conditions. In the c.w. condition, no nanoprecipitates were present in the bulk nor in the irradiated layer, hence DF images using these imaging conditions did not show any interesting contrast. No reflections of other precipitating phases were found in diffraction patterns from the irradiated layer.

Fig. 2 shows ion maps from a 5 nm thick vertical slice through an APT measurement from the irradiated layer of the aged material. The microstructure was dominated by clusters of Si and Ni. At the locations of these clusters Cr and Fe were depleted. The clustering of Si and Ni is likely the result of radiation induced segregation towards extended defects, such as dislocations and Frank loops. Very small clusters of Ti could also be observed, but there was no apparent correlation with C. This is further illustrated in the inset of Fig. 2, which shows a zoom of the slice with only Ti, C and Si ions plotted. Many Si clusters coincided with the small Ti clusters. In general, Ti clusters always showed visible Si enrichment, but the reverse was not always the case. Ion maps from the irradiated layer in the c.w. material showed identical behavior for all elements. This demonstrates that the small Ti clusters in both materials formed during the irradiation and are not all remnants of TiC nanoprecipitates originally present in the aged material.

Results from an APT measurement containing a boundary are shown in Fig. 3. This sample was taken from the irradiated layer in the c.w. material. Fig. 3(a) shows the Si ion map together with a 4 at% Si isosurface. The isosurface serves to illustrate the presence of the boundary, as well as other Si-enriched defects such as a dislocation segment.
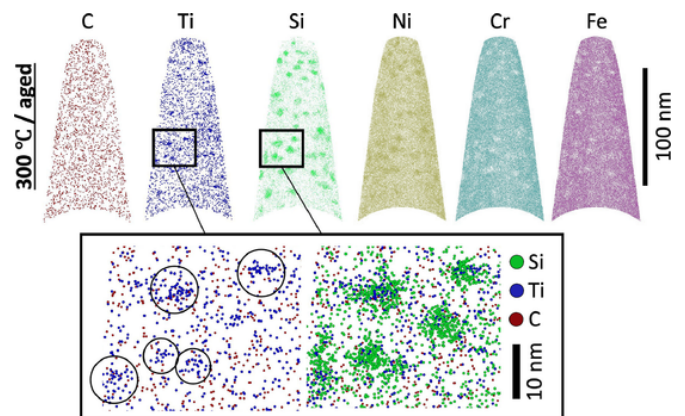

Fig. 2. Ion maps of C, Ti, Si, Ni, Cr and Fe from a 5 nm thick vertical slice of an APT measurement from the irradiated layer in the aged material (irradiated at 300 °C). The inset shows a zoom of a marked region and indicates that the Ti clusters were also enriched with Si. Conversely, not all Si clusters showed strong Ti enrichment. Visually, Ti clusters did not appear correlated with C clusters.
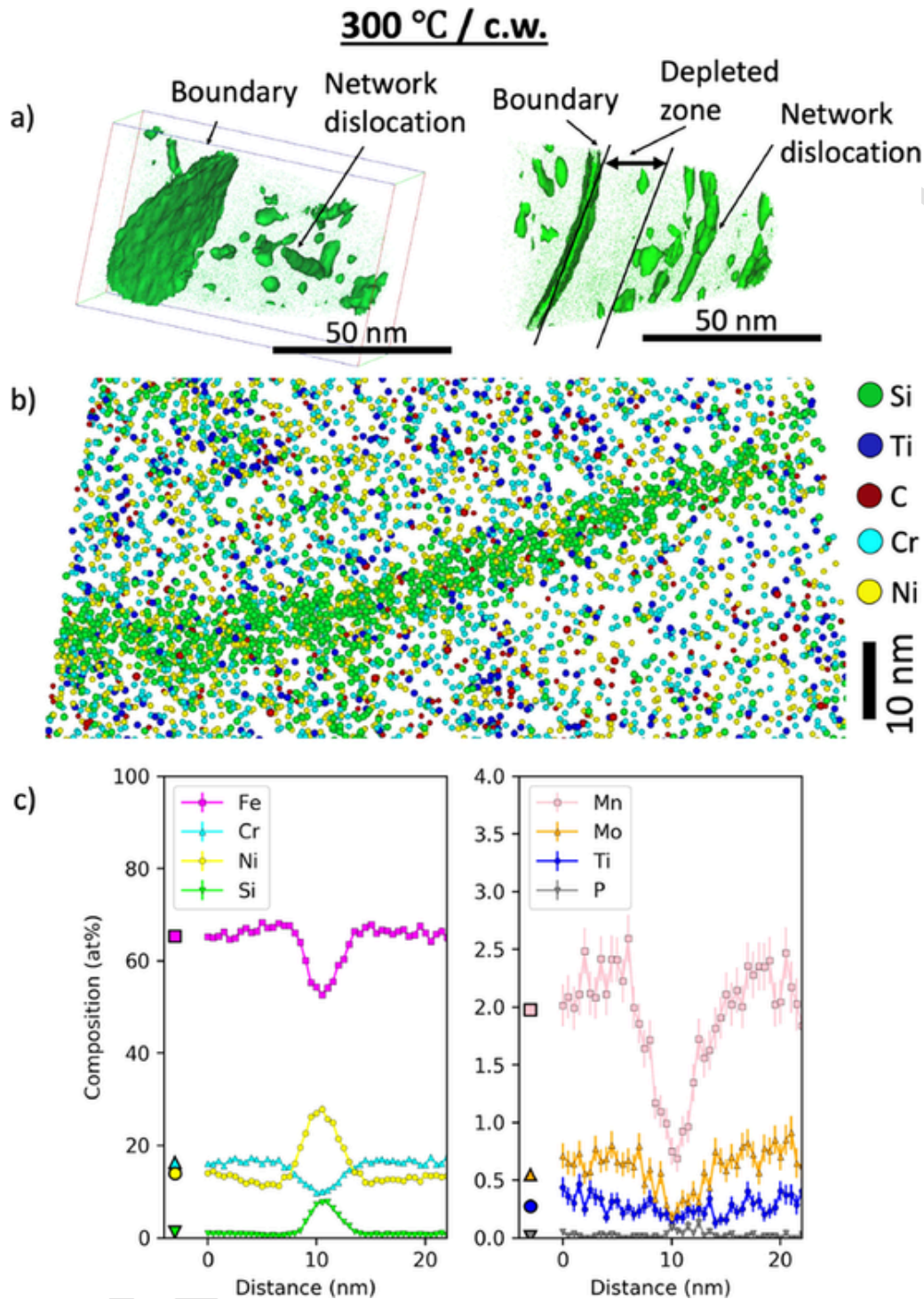
Fig. 3. (a) APT sample from the 300 ℃/c.w. condition showing the Si ion map with 4% Si isosurfaces. The sample shows an Si-enriched boundary. The boundary shows a cluster depleted zone of about 20 nm. (b) A detailed ion map of a slice through the boundary, showing Si and Ni enrichment but no Ti enrichment. (c) The composition profile across the boundary. The larger markers on the left correspond to the bulk concentration measured by APT in the pristine c.w. steel.

A thin zone next to the boundary was void of Si clusters because boundaries are strong sinks for point defects. This means that the neighboring region was depleted in these defects, which inhibited the formation of clusters. Fig. 3(b) shows a more detailed ion map of a slice through the boundary. Si and Ni were strongly enriched but Ti was not. This is also shown in the composition profile through the boundary in Fig. 3(c). Si, Ni, and P were enriched at the boundary, while Fe, Cr, Mn, and Mo were depleted. The composition of Ti was nearly unaffected by the boundary. This suggests that the Ti clustering observed in Fig. 2 did not occur via RIS.

In the line-profile approach, the counting statistics were insufficient to draw strong conclusions about the behavior of minor elements such as C, B and V, although it did appear B was slightly enriched at the boundary. To make some inference about the behavior of these minor elements, averaged proxigrams from multiple Si isosurfaces were constructed. While no meaningful quantitative conclusions could be drawn

from such analysis, all samples showed that on average C and B tended to co-enrich with Si, while V tended to be depleted. Hence, while it is not visually obvious from the ion maps, this indicates that some of the Ti clusters might be small nuclei of TiC. An example of such an averaged proxigram is given in the supplementary materials.

The number density of small solute clusters was estimated with two methods. Because Si showed the strongest segregating behavior, it was chosen as the element to classify the clusters. In the first method, the number of volumes enclosed in the 4 at% Si isosurfaces were counted. This method only captured the somewhat larger clusters of at least a few hundred atoms. Surfaces that did not encompass a closed volume represented a cluster at the boundary of the sample and were counted as only half a cluster. The second method used the 2-step k-nearest neighbor (KNN) clustering algorithm implemented in 3Depict to isolate and count the clusters. In the clustering algorithm, Si was used as core element and a 10 atom cluster size cut-off was used. The parameters for the clustering algorithm were estimated from the nearest neighbor statistics. In both methods, the cluster counts were assumed to follow Poissonian statistics so the uncertainty was taken to be the square root of the count. The total volume of the needle was estimated from the convex hull. The uncertainty on the volume was taken to be 10%, in line with the variation in the number of atoms/volume between the different samples due to the uncertainty in the reconstruction parameters. Results are summarized in Fig. 2 and represent the volume weighted average of two independent APT measurements from each irradiation condition.

The number density tended to be almost two times higher in the KNN method due to the detection of small clusters and the inability to detect whether clusters are on the edge of the sample. Hence, the KNN method yielded an overestimation of the cluster number density, while the isosurface method yielded an underestimation. There is no significant difference between the number of clusters in the c.w. and aged condition; both conditions showed a cluster density between $3 - 6 \times 10^{23}$ m^{-3} depending on how the clusters were counted.

Constructing size distributions of clusters was not attempted since the bounds of the clusters were ambiguous. Some isolated features were in the same size range as Frank dislocation loops that were observed by TEM (about 5–10 nm).

Overall, for the chosen irradiation conditions at 300 °C, the microstructure prior to irradiation has very little impact on the post-irradiation microstructure. The fact that both the aged and c.w. material look identical after irradiation suggests the material has evolved to a steady state microstructure.

3.2. Elevated irradiation temperatures: 450 °C and 600 °C

Irradiation at 450 °C and 600 °C also lead to Ni and Si clustering as was the case at 300 °C. In contrast, higher temperature irradiations lead to the formation of distinct Ni-Si precipitates, which were detected both by APT and TEM. Additionally, Ti-C clusters were detected in all the samples. The samples irradiated at 450 °C and 600 °C differed mostly in terms of the size, number density and volume fraction of

these radiation induced precipitated phases. Hence all these irradiation conditions are treated together in this section.

3.2.1. Atom probe tomography study of precipitates

Fig. 4 shows ion maps for a 5 nm thick cross section through an APT measurement taken from the 450 °C/aged material. TiC clusters are circled in red, Ti-Ni-Si clusters are circled in green. Both types of clusters were depleted in Fe and Cr. Detailed ion maps of each type of cluster are shown in the insets. The interfaces of the TiC clusters were decorated with Si and Ni. The Ni-Si-Ti clusters showed an abrupt depletion in Cr and Fe and no obvious internal composition gradients, suggesting these clusters were a precipitated phase. The particles were also enriched in Mn, and were surrounded by an Mn depleted layer as shown in the inset. The presence of Mn in the clusters suggests these were G-phase precipitates [32,46]. G-phase precipitates could be distinguished from other Ni and Si clusters in this way, since Mn is normally depleted by RIS. The same microstructural features were observed in the c.w.-material irradiated at 450 °C and both materials irradiated at 600 °C. However, features were coarser at the higher irradiation temperature, especially for the aged material. Additional ion maps of these measurements are given in the supplementary materials.

Fig. 5 shows detailed ion maps of slices through G-phase and TiC clusters. In the top-left corner of Fig. 5(a) a well defined TiC particle coated with a shell of Si and Ni is shown. Slightly left of the center in Fig. 5(a), a G-phase particle is shown which was not attached or otherwise associated with a carbide particle. Likely this particle grew by Ni and Si accumulation on a dislocation loop. However, many G-phase particles grew directly on TiC particles, as shown in Fig. 5(b). The Mn depleted layer around the G-phase precipitate is indicated in the image. The yellow arrows in Fig. 5(a) point to Ti-C clusters that appear to have been infiltrated by Si and Ni. Possibly, these were very small TiC clusters with a Ni and Si enriched shell. It could also be that these TiC particles were transforming to G-phase particles directly; this might explain the enrichment of Ti and occasionally the enrichment of C observed in G-phase particles.

The enrichment of Si and Ni and the formation of G-phase particles on the TiC interfaces is further illustrated by the proxigram in
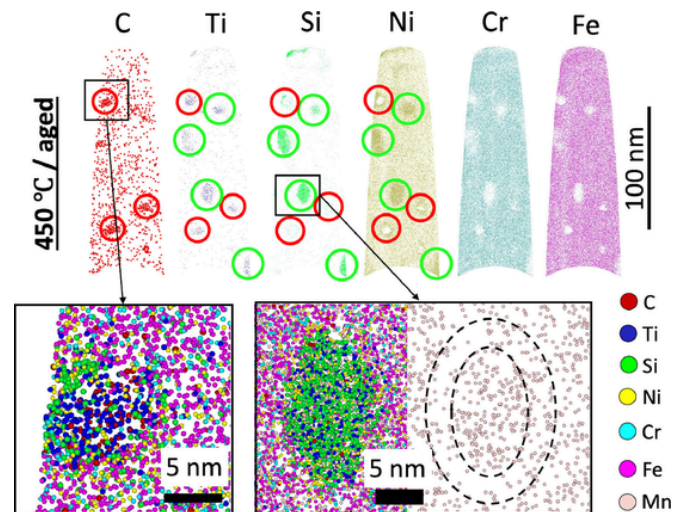

Fig. 4. Ion maps of a 5 nm thick vertical cross-section through an APT measurement taken from the aged material irradiated at 450 °C. Ti-C and Si-Ni-Ti clusters are circled in red and green respectively. The insets show two detailed ion maps of both cluster types. The edges of TiC clusters were decorated with Si and Ni, indicating enrichment at the interface. The Si-Ni-Ti clusters represented G-phase as evidenced by the presence of Mn. The detail Mn ion map of the precipitate shows enrichment inside the particle and a depleted layer surrounding the particle. These features are marked with dashed lines. (For interpretation of the references to colour in this figure legend, the reader is referred to the web version of this article.)

Table 2
Si cluster number densities in material ion irradiated at 300 °C estimated from the 4% Si isosurfaces and the KNN technique in different APT samples. The parameters used in the KNN method were: core classify distance of 1.5 nm, core link distance of 1 nm, bulk link distance of 0.5 nm, erosion distance of 0.4 nm, minimum cluster size of 10 ions.

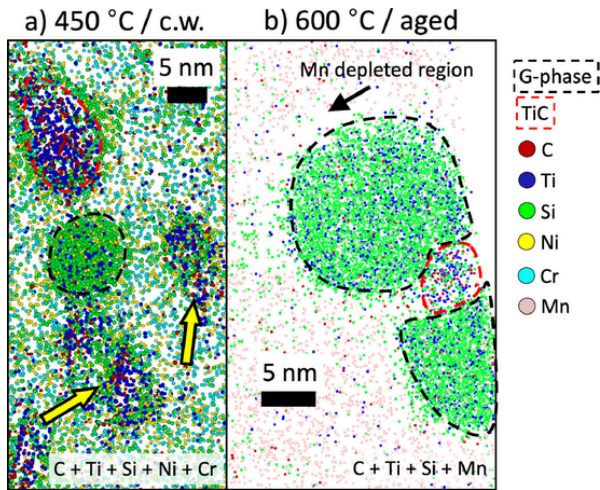| Condition	Number density (4% Si)	Number density (KNN)
	10^{23} m^{-3}	10^{23} m^{-3}
c.w.	3.5 ± 0.4	6.0 ± 0.7
aged	3.1 ± 0.4	5.6 ± 0.7

Fig. 5. Detailed ion maps showing examples of G-phase and TiC precipitates in cross section in the (a) 450 °C/c.w. and (b) 600 °C/aged condition. In (a), slightly left of the center, a G-phase precipitate is circled with a black dotted line. It did not appear attached to any carbides. Yellow arrows point to TiC clusters that appeared to have been infiltrated by Si and Ni. These clusters could be very small TiC particles decorated with Ni and Si or TiC clusters in the process of converting to G-phase. (b) G-phase particles that grew on the interface of a TiC particle.

Fig. 6(a). The proxigram was constructed by considering all 10 at% C isosurfaces in order to smooth the profile. The plateau at distances > 0 suggests the clusters tended towards a stable composition in their interior, confirming they were a precipitated phase. The carbides were enriched in Cr, Ti, Mo, as well as in V and B of which the profiles are not shown. The apparent contradiction between the ion maps of Fig. 4, where Cr appears depleted in TiC clusters, and the proxigram, which shows Cr to be enriched inside the clusters, can be explained by the observation that the atomic density was a factor 2–3 lower in the carbides compared to the matrix. This is partly due to differences in evaporation field between the phases, which artificially magnifies the carbides, as well as multiple correlated evaporation events happening in the carbides during a single pulse which go undetected [47]. The peak in the Si and Ni profiles just below distance 0 shows that the interfaces of the carbides were enriched with these elements. Fe and Cr show a dip in the same place. Both these observations are in line with expected RIS behavior.

Fig. 6 (b) shows the proxigram constructed from a 10 at% Si isosurface. Since G-phase precipitates were larger than the carbides and showed a similar atomic density as the matrix, this proxigram was constructed from a single large particle. It shows that the G-phase particles were enriched in Ni, Si, Mn, Ti and slightly in P. The Mn profile shows a dip near the interface, indicative of the depletion layer also shown in Fig. 4. The proxigrams in Fig. 6 originate from the aged material irradiated at 600 °C; similar curves showing the same trends were obtained in the other high temperature irradiation conditions.

The composition of the carbides and silicides were estimated by separating ions with an appropriate isosurface, then performing a peak decomposition algorithm on these ions. The isosurface parameters were set so that a minimum of Fe (which is depleted in both phases) but a maximum of the relevant ions were captured. The results are summarized in table 3. For the carbides this compromise was around 10 at% C. Due to limited statistics within single particles, the inter-cluster differences in composition were large. According to the output from the peak decomposition algorithm, the composition was between 25–30 at% C, 22–30 at% Ti, 30–36 at% Cr, 4–9 at% Mo and 1–3 at% of Ni and Fe. Ni and Fe were probably erroneously included and belonged to the surrounding matrix. The measured carbon content should not be interpreted quantitatively since carbon content of carbides tends to be significantly underestimated [47]. However, compared to the carbides formed by ageing (see Section. 2), the composition of the irradiation induced carbides was substantially different: they contained about half the amount of Ti and Mo and about three times more Cr. Differences between the different irradiation conditions were modest in comparison to the large inter-cluster spread. However, the 600 °C/aged irradiation condition showed carbides with a slightly higher Ti and Mo content but a lower Cr content compared to the other irradiation conditions. Since this composition is closer to the composition of the carbides in the non-irradiated aged material, this suggests that remnants of the original thermally induced precipitates were still present in this condition.

The G-phase particles showed a more narrow compositional distribution: 23–27 at% Si, 51–53 at% Ni, 3–5 at% Ti, 4–5 at% Cr, 4–7 at% Mn, and 6–7 at% Fe. The ions that yielded this estimation were captured with a 20 at% Si isosurface. These composition values are consistent with earlier reports [32]. The phase also showed traces of B, P and C particularly at 600 °C. All elements that are known to enrich at sinks by RIS were incorporated in the G-phase: Ni, Si, B, and P. The presence of Mn in the G-phase seems contradictory to its tendency to deplete near sinks via RIS. The behavior of Ti was also anomalous: Ti did not appear to enrich by RIS at 300 °C, but at higher irradiation temperatures it was co-enriched in all Si-Ni clusters. Interestingly, while G-phase is known to be accommodating for most transition metal elements [46], Mo was found to be almost completely absent.
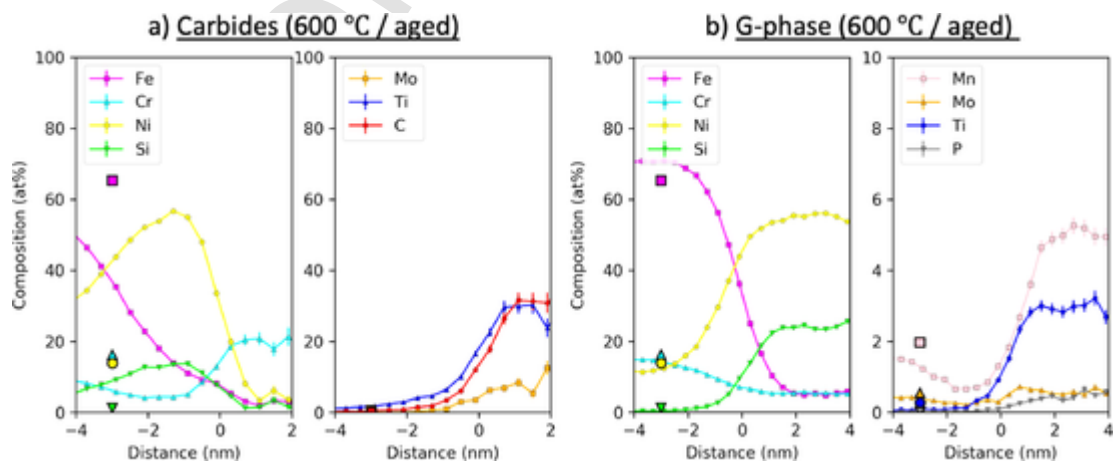

Fig. 6. Proxigrams in the 600 °C / aged condition constructed from the (a) aggregate 10 at% C isosurfaces and (b) the 10 at% Si isosurface surrounding one large G-phase precipitate. The isosurface values were selected such that the composition profile inflection point was approximately aligned with distance zero.

Table 3

Summary of precipitate compositions in the 450 °C and 600 °C irradiated conditions estimated from APT measurements. The uncertainty represents the standard error on the mean composition computed from several precipitates.

	Carbides				G-phase			
Irrad. temp.	450 °C		600 °C		450 °C		600 °C	
Initial state	aged	c.w.	aged	c.w.	aged	c.w.	aged	c.w.
B (at%)	trace	trace	trace	trace	trace	trace		trace
C (at%)	32 ± 6	30 ± 4	25 ± 2	27 ± 2			trace	trace
Si (at%)			1.4 ± 0.3	1.0 ± 0.1	26.6 ± 0.8	25 ± 1	23.5 ± 0.5	23.3
P (at%)				trace	trace	trace	trace	trace
Ti (at%)	24 ± 2	22 ± 2	30 ± 4	21.7 ± 0.8	3.9 ± 0.3	3.0 ± 0.6	5 ± 1	2.5
V (at%)	trace	trace	trace	trace				
Cr (at%)	31 ± 5	36 ± 3	27 ± 4	34 ± 1	4.5 ± 0.4	4.6 ± 0.8	5.3 ± 0.1	5.3
Mn (at%)	1.0 ± 0.8				5.4 ± 0.4	6.8 ± 0.6	3.8 ± 0.7	5.6
Fe (at%)	3 ± 1	5 ± 1	2.8 ± 0.4	4 ± 1	5.8 ± 0.5	5.9 ± 0.7	6.5 ± 0.7	11.6
Ni (at%)	3 ± 1	3 ± 1	4.0 ± 0.8	4 ± 1	53.8 ± 0.9	54 ± 2	54.0 ± 0.8	51
Mo (at%)	6 ± 1	4 ± 1	9.0 ± 0.5	7.3 ± 0.8			trace	

3.2.2. TEM investigation of precipitates

TEM selected area diffraction combined with dark field imaging supported the presence of MC-type and G-phase precipitates. Fig. 7(a) shows a close up of a selected area diffraction pattern (SADP) taken in the irradiated layer of the 450 °C/aged condition. The sample was tilted to the $(002)_\gamma$ 2-beam condition, strengthening the intensity of reflections along the $(002)_\gamma$ direction, including reflections of secondary phase particles with specific orientation relationships to the matrix. The TiC 002 reflection was faint because there was a brighter reflection nearby which was identified as the G-phase 006 reflection. The DF image obtained by only including the TiC reflection inside the objective

aperture is shown in Fig. 7(c). The other bright reflections, including the bright reflection adjacent to $(002)_{TiC}$, correspond to the G-phase 004 and 006 reflections (3.5 and 5.3 1/nm respectively). From these diffraction spots, the G-phase lattice parameter was measured to be 1.14 ± 0.04 nm, which corresponds well to literature values [46,48]. The DF images using the $(004)_G$ and $(006)_G$ reflections are shown in Fig. 7(b) and (d) respectively. In Fig. 7(d), signal from TiC was included in the image because the $(002)_{TiC}$ reflection could not be excluded from the objective aperture. The images show similar features, confirming that the two reflections originated from the same phase. The G-phase precipitates in these images formed with an orientation relationship that includes the condition $\langle 100 \rangle_\gamma \| \langle 100 \rangle_G$, possibly cube-on-
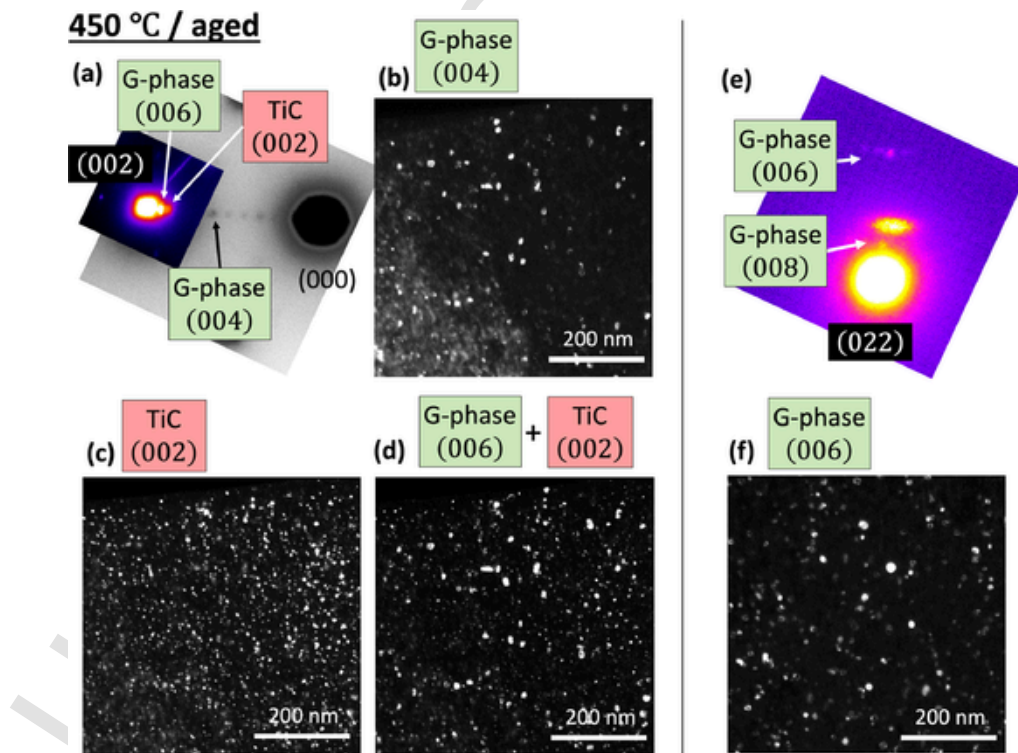

Fig. 7. Selected area diffraction patterns (SADP) and dark field images from the irradiated layer in the 450 °C/aged condition. (a) The SADP in the $(002)_\gamma$ 2-beam condition with the diffraction spots corresponding to TiC and G-phase marked. DF images using the (b) G-phase 004, (c) TiC 002, and (d) G-phase 006 plus TiC 002 reflections. (e) A close up of the SADP in the $(022)_\gamma$ 2-beam condition. (f) DF image using the G-phase 006 reflection.

cube as reported in [49]. Additional faint spots can be seen between the aforementioned reflections. DF imaging using any of these faint spots did not reveal additional features, indicating that they were the result of double or multiple diffraction.

Diffraction experiments along other zone axes or 2-beam conditions, most notably $g = (022)_\gamma$, suggested that the G-phase precipitates exhibited multiple different orientation relationships with the austenite. A SADP in this diffracting condition is shown in Fig. 7(e). Two sets of reflections corresponding to $(006)_G$ and $(008)_G$ are marked. These reflections were closely, but not precisely, aligned with the $(022)_\gamma$ direction. This is inconsistent with a cube-on-cube orientation relationship but would be consistent with a Kurdjumov-Sachs (KS) orientation relationship, as was already suggested for G-phase in [50]. The DF image corresponding to the $(006)_G$ reflection in this diffraction pattern is shown in Fig. 7(f). No evidence was found of phases other than TiC or G-phase; in terms of $|g|$ all diffraction spots could be attributed either to TiC or to G-phase with a lattice parameter of 1.14 ± 0.04 nm. No evidence was found for the presence of γ', which would manifest as a $(001)_{\gamma'}$ reflection halfway between (000) and $(002)_\gamma$.

Fig. 8 (a) and (b) show a side-by-side comparison of DF composite overview images using the $(002)_{TiC}$ reflection in the 450 °C/ c.w. and aged conditions, respectively. In the c.w. sample, the extent of the irradiated layer is demarcated by the presence of the nanoprecipitates, demonstrating that irradiation is responsible for their formation. Note that in this image series, the first 500 nm shows a large primary TiC particle in a non-diffracting condition which contains no small particles and hence shows no contrast in DF. In other regions of the sample, where the matrix bordered the surface, the same TiC nanoprecipitates were observed. In the aged sample, the morphology of the precipitate population in the irradiated layer (<800 nm) looks different compared to the initial population visible beyond the irradiated layer (>1500 nm). The original precipitate population reflects the initial cellular dislocation network, which was no longer visible in the population of the irradiated layer. This indicates a new population of particles grew, possibly replacing some or all of the old population.

In the aged sample, the TiC contrast appears weaker beyond about 800 nm from the surface. Given that the nanoprecipitate-depleted band is not parallel to the irradiated surface, the matrix intensity is stronger in this region, and the particle intensity gradually fades out at 800 nm
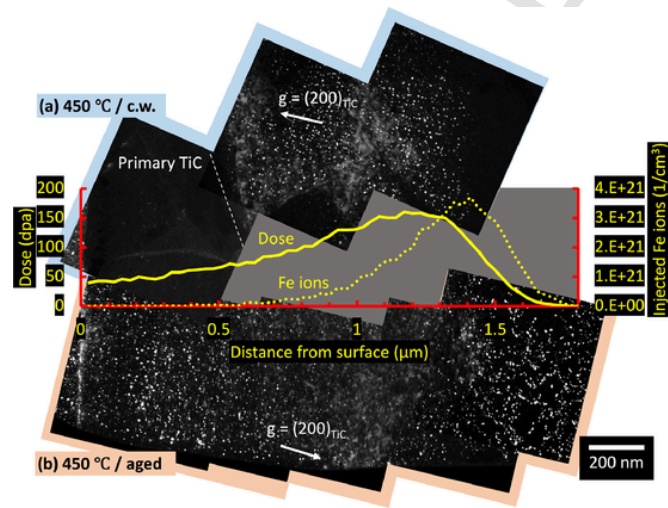
and back in around 1.1 μm, the most likely explanation is that this is a Bragg artifact due to local bending of the sample. If it is a real effect, this would imply the particles are sensitive to the dose, the dose rate, or the beam injected Fe ions. In this case, a similar gradient would be expected in the c.w. material, which was not observed. However, it could be that some of the features in image 8(a) are G-phase precipitates via $(600)_G$ since the aperture position could not be calibrated based on the $(002)_{TiC}$ reflection in the non-irradiated bulk. This would conceal an MC gradient in the c.w. material. This feature was not investigated more in detail and the rest of the characterizations focus on the first 500 nm.

3.2.3. Quantification of precipitate populations

Both the APT and TEM data was used to estimate the average size, number density and volume fraction of the precipitated phases in the different irradiated conditions. The results for irradiation conditions at 450 and 600 °C are summarized in Fig. 9, and also in tables in the supplementary materials. No well-defined precipitates were detected after irradiation at 300 °C so this temperature is not included in the plots.

To estimate size and number density with APT, the isosurface method as described in Section 3.1 was employed. The clusters that qualified as precipitates were large enough to be detected this way. The isoconcentration values chosen were 4 at% C for the carbides and 20 at% Si for the G-phase particles. To estimate the number density, open volumes (due to the precipitate being on the edge of the sample) were counted as half clusters. The volume of the entire sample was estimated with the convex hull method. The uncertainty was derived from an assumed 10% uncertainty on the reconstruction volume and the uncertainty on the count. The radius of each cluster r was estimated with Eq. 1, which assumes that each cluster can be approximated by a sphere. Only clusters that could be surrounded by a closed volume isosurface were used in the calculation. The standard error on the mean radius serves as the uncertainty. The volume fraction was estimated in two ways, with Eq. 2 and Eq. 3. Eq. 2 estimates V_f in an indirect way based on the average radius $\bar{r}$ and the number density N_d. Errors are propagated from uncertainties in both these values. Eq. 3 calculates the volume fraction in a more direct way by taking the ratio of atoms inside isosurfaces N_p and all atoms in the sample N_{tot}, multiplied by a factor f_v that expresses the ratio between the average atomic density and the atomic density of the precipitates. The value f_v was estimated by calculating the atomic density of various selections inside the precipitates and inside the matrix. For the carbides $f_v = 3 \pm 0.6$, for the G-phase $f_v = 1 \pm 0.2$. If multiple APT samples of the same condition were available, their information was combined (sum of volume, sum of clusters, sum of atoms). In each condition, the number of clusters counted for each phase varied between 5–60, the total number of atoms was around $1 - 4 \times 10^7$, and the sampled volume was around $4 - 11 \times 10^5$ nm^3.

$$r = \left(\frac{3V}{4\pi} \right)^{\frac{1}{3}} \tag{1}$$

$$V_{f,1} \approx \frac{4}{3} \pi \bar{r}^3 N_d \tag{2}$$

$$V_{f,2} = f_v \frac{N_d}{N_{tot}} \tag{3}$$

The number density, average size and volume fractions of the different precipitates were estimated from TEM DF images by grey-value thresholding the images and running an automated particle sizing script in ImageJ. DF images were made with the $\{002\}_{TiC}$ and $\{006\}_G$ reflections using the $\{002\}_\gamma$ and $\{022\}_\gamma$ 2-beam conditions respectively. The thickness of the samples was estimated with the EELS log-ratio method [51–53]. The inelastic mean free path implemented in the
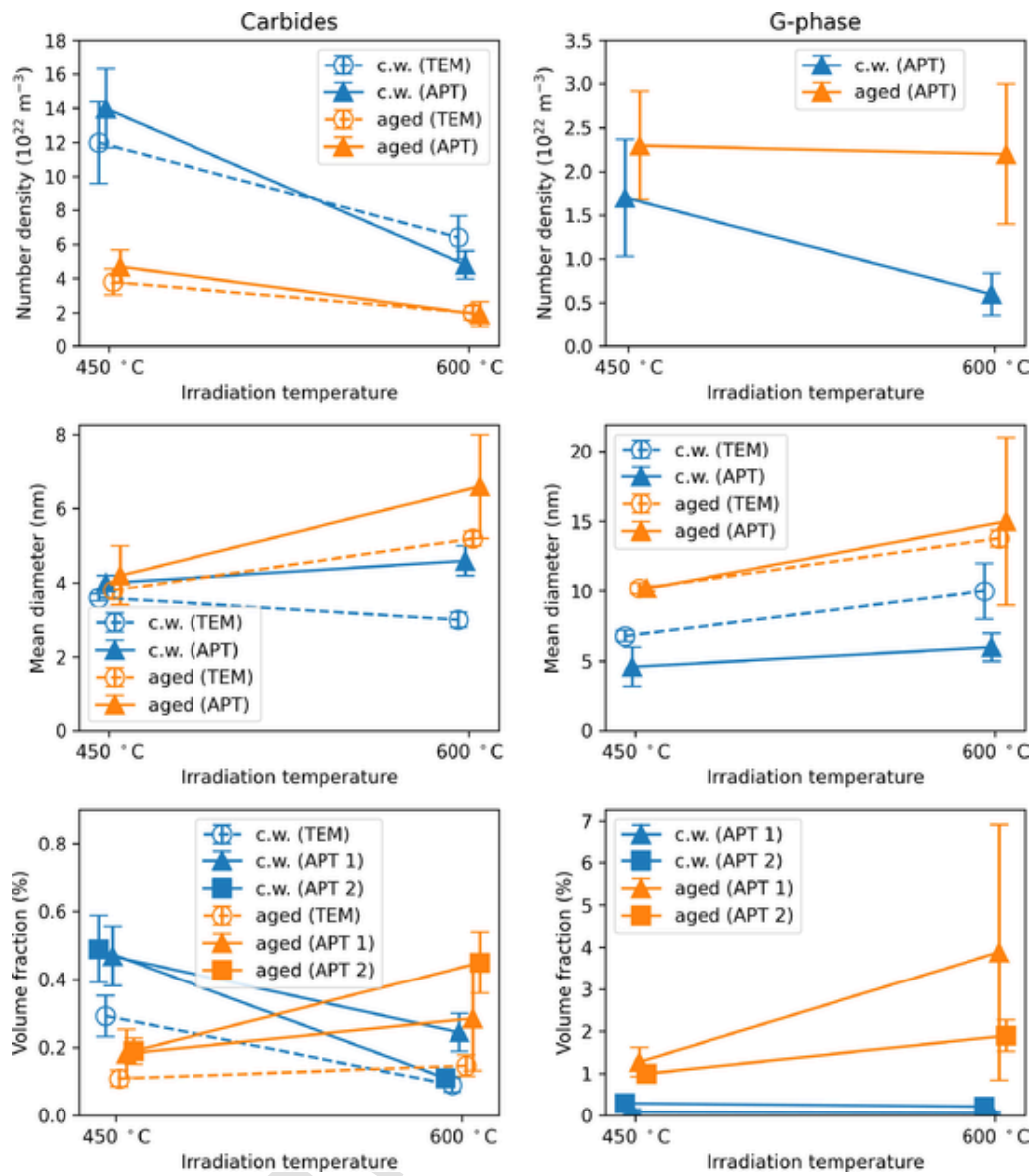

Fig. 8. Composite DF image using $(200)_{TiC}$ of a cross section of the irradiated layer in the (a) c.w. and (b) aged samples irradiated at 450 °C. The SRIM dose and injected Fe ion profiles are superimposed on the image. In (a), a large primary TiC particle is located at the surface of the sample, which in this image series unfortunately hides the fact that there were also small TiC precipitates in the first 500 nm of the irradiated layer in other regions of the sample where matrix borders the surface.

Fig. 9. Summary of number density, mean diameter and volume fraction of carbides and G-phase particles in the 450 ℃ and 600 ℃ irradiated conditions, estimated by APT and TEM. Points are slightly offset in the x-direction to improve visibility. The first row of plots represents the number density, the second row the mean particle diameter, the third row the volume fraction. Results on the carbides are plotted in the first column of plots, results on the G-phase is in the second column. The volume fraction was estimated in 2 ways from the APT results: APT 1 represents equation 2, APT 2 represents equation 3. The TEM estimates of the G-phase number density and volume fraction are not plotted due to the unknown multiplicity factor.

EELS toolbox of Digital Micrograph was used. An uncertainty on the thickness of 20% was assumed. To calculate the mean size, the smallest features considered were 2 nm in diameter. The error bar represents the standard error on this mean. For the volume fraction, equation 2 was again used. To avoid confusion, the G-phase number densities and volume fractions as estimated by TEM are not shown in Fig. 9. Due to the various possible orientation relationships and the multiple variants contributing to one image, the raw count in any DF image represents a significant underestimation that needs to be corrected for with an unknown factor. Indeed, the number density calculated from this raw count was consistently 2–4 times smaller than the estimate derived from APT. The raw count values are given in tables 2 and 3 in the supplementary materials; they show the same trends as the APT results.

By most measures, the TEM and APT estimates are in reasonable agreement; volume fractions differed most due to the r^3 dependence. Still, when comparing different irradiation conditions, trends were the same for both methods.

The plot shows significant discrepancies in MC number densities in the different irradiated conditions. In both the 450 ℃ and 600 ℃ irradiations, there were about three times more carbides in the c.w. material compared to the aged material. At 450 ℃ there were about 2 times more carbides compared to 600 ℃ for both materials. The mean diameter of the carbides was comparable for most conditions, though it appeared slightly larger in the 600 ℃/aged condition. This may be due to some particles being remnants from the slightly larger original nanoprecipitate population present in aged material, skewing the average upwards. Differences in volume fraction are minor and for all conditions values ranged between 0.1 to 0.5 vol%. At 450 ℃ the c.w. material showed a higher volume fraction than the aged material due to the significantly higher number density yet comparable size; at 600 ℃, the aged material shows a slightly larger volume fraction than the c.w. due to the larger particles that compensate for the lower number density.

The G-phase number density was higher in the aged samples compared to the c.w. samples, especially at 600 ℃. For both irradiation

temperatures, G-phase particles in the aged material were about two times larger than those in the c.w. material. These factors combined yield substantial differences in the volume fraction of G-phase, which was consistently 3–10 times higher in the aged samples compared to the c.w. samples.

4. Discussion

Samples of Ti-stabilized austenitic steel irradiated with Fe ions in different conditions were characterized and quantified with APT and TEM. To illustrate the rest of the discussion, overview diagrams of the microstructural evolution are given in Fig. 10.

Prior to irradiation, the microstructure in the c.w. material is characterized by a homogeneous solid solution and a dense dislocation network. The Ti concentration in solid solution is high at about 0.3 at%, which is illustrated in Fig. 10 (a) by the dark blue hue. In the aged material Fig. 10 (b)), Ti is clustered into MC nanoprecipitates which grew on dislocations. The matrix concentration of Ti is reduced to about 0.1 at% and the dislocation density is also slightly reduced. After irradiation at 300 °C, both materials evolved to a similar microstructure characterized by an absence of MC precipitates and the presence of fine scale clustering of Si and Ni (represented by green clouds in Fig. 10 (c) and (d)). Many of these clusters are enriched in Ti, which is represented with blue dots in the figure. The Ti concentration in solid solution is again close to 0.3 at% due to the redissolution of the particles and the redistribution of solute. After irradiation at temperatures of 450 and 600 °C Fig. 10 (e) and (f)), the microstructures in both the c.w. and aged materials contain MC precipitates. Si and Ni segregated to the interface of the nanoprecipitates. G-phase, a nickel silicide enriched in Ti and Mn, was also identified in both microstructures, often attached to MC precipitates. The number density of the MC nanoprecipitates was much greater in the c.w. material than in the aged material. In the same condition, the G-phase particles were less numerous and smaller. In both cases, the Ti content in solid solution is close to 0.1 at%. After irradiation, all the microstructures were also characterized by a population of dislocation loops as well as a dense dislocation network typical for austenitic steel irradiated beyond 10 dpa [54].

The nucleation and growth of G-phase is the result of radiation induced segregation. In all experiments, the same elements segregated to lattice defects due to irradiation: Si, Ni, P, and sometimes B. These observations are in line with a large body of work on 304 and 316 steels [27,29,34,55,56]. All these elements are major constituents of G-phase. The segregation of Si and Ni to the interfaces of MC precipitates in the materials irradiated at 450 and 600 °C demonstrates that these precipitates are acting as sinks or point defect recombination centers. Due to their absorption or annihilation of radiation induced point defects, sinks and point defect recombination centers have a reduced point defect concentration in their direct vicinity compared to the bulk. A point defect concentration gradient develops which, via Fick's law, leads to point defect fluxes towards the sink. This point defect concentration gradient is illustrated in Fig.s 10 (g) and (h) by the pink dotted lines. If there are more sinks, more point defects can be accommodated and the point defect concentration in the bulk is reduced, leading to smaller gradients and fluxes near sink interfaces. In the c.w. material there are more MC precipitates both at 450 and 600 °C. Assuming they act as perfect unbiased sinks, classical rate theory [57] combined with the values from Fig. 9 predict that the bulk vacancy concentration is 3–5 times higher in the aged material compared to the c.w. material. The details of this calculation can be found in the supplementary materials. Due to the preferential exchange of point defects with some types of atoms in the alloy, concentration gradients of certain elements build up near sinks mirroring the point defect gradients. This is the basis of the RIS effect. Quantitative prediction of RIS profiles in complex alloys such as stainless steels is currently not possible, as it depends on each elements' exchange rate with two types of point defects and multiple unknown activity coefficient functions. However, at the same irradiation temperature, a stronger gradient of point defects leads to higher fluxes, which leads to steeper RIS profiles. This provides an explanation for why more G-phase formed in the aged material as compared to the c.w. material. As illustrated by the green lines in Fig.s 10 (g) and (h), the Si and Ni concentration profiles near the interface of sinks mirrors the point defect concentration profile. Hence in the aged condition, the concentrations of Si and Ni near the interface are higher. At a certain composition, the solubility of Ni and Si in the matrix is exceeded and the formation of radiation induced phases such as G-phase is initiated. This event is much more likely in the aged material, which explains the higher volume fraction of G-phase at 450 and 600 °C compared to the c.w. material.

Whereas in non-stabilized steels γ' phase tends to dominate over G-phase [46,58], G-phase was the only nickel silicide found in this material. At 450 and 600 °C, Ti co-segregated with Ni and Si and was strongly enriched in G-phase. This suggests that the presence of Ti strongly favors G-phase formation over γ'. The RIS behavior of Ti is
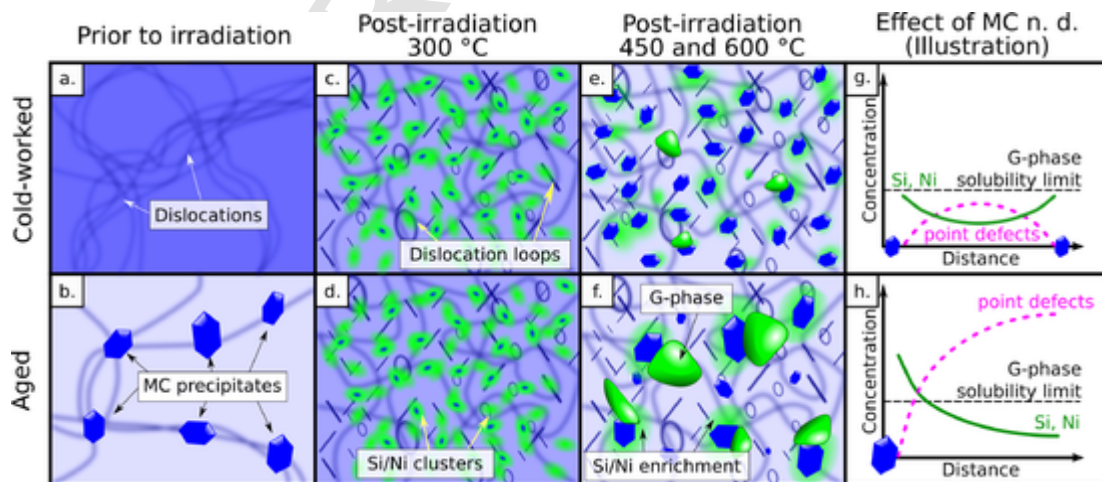

Fig. 10. Diagrams to illustrate the microstructural evolution in Ti-stabilized steel under irradiation. The first column represents the pre-irradiation microstructures in the (a) c.w. and (b) aged materials. The second column represents the microstructures of the (c) c.w. and (d) aged materials after irradiation at 300 °C. The third column represents the microstructures of the (e) c.w. and (f) aged materials after irradiation at 450 and 600 °C. In (a), (b), (c), (d), (e), and (f), the blueness of the background represents the amount of Ti in solid solution. The relationships between MC number density, point defect concentrations, RIS gradients and G-phase formation after irradiation at elevated temperature are illustrated in (g) and (h) for the c.w. and aged materials respectively.

anomalous. A general rule of thumb in RIS is that undersized atoms segregate towards sinks whereas oversized atoms segregate away from sinks. For example, in austenite, Ni is undersized whereas Cr and Ti are oversized. The enrichment of Ti at sinks could be testament to the complex dependence of RIS on each element's activity coefficient, which in turn depends on local composition. At low irradiation temperature (300 °C) there was no sign of Ti enrichment on a grain boundary. Perhaps this can be explained by changing diffusion mechanisms. At 300 °C, only self-interstitials are mobile and contribute to diffusion. This is evidenced by the fact that small atoms such as Si, P and B, which primarily diffuse via interstitials [29,33], show much higher enrichment factors at low temperatures compared to large atoms such as Ni. Ni is also known to have some diffusivity via interstitials, but like Fe and Cr it mostly diffuses via vacancies (the inverse Kirkendall mechanism) [59]. The large Ti atoms may require mobile vacancies to diffuse, which would explain why it does not co-segregate with Si and Ni at low temperature. The fine clustering of Ti at 300 ° in the c.w. material could reflect Ti diffusing very short distances to the cores of cascades, which are typically very rich in vacancies. The absence of G-phase at 300 °C can then be primarily attributed to limited vacancy diffusion, which prevents the formation of significant gradients of elements such as Ni and Ti.

Besides Ti, Mn was significantly enriched in G-phase. Contrary to Ti, Mn always showed the tendency to deplete near sinks via RIS. This suggests G-phase requires Mn in order to be stable. A possible way to avoid G-phase formation then could be to reduce the Mn content in the alloy. However, this might also come at the cost of reduced strength and hardenability.

While voids were not observed in the materials studied in this work, in the past G-phase formation has been linked to uncontrollable void swelling and microstructural instability [26,60,61]. Hence it is generally considered an undesireable phase. The results in this work indicate that maximizing the number density of MC is an effective strategy to minimizing G-phase.

To explain the observed MC precipitate behavior, they can be modeled as a thermal phase with growth kinetics that are enhanced by radiation. In the absence of radiation, solubility of TiC in austenite is very low [62] and the formation of nanoprecipitates tends to be limited only by sluggish diffusion. In a previous study [40], the c.w. material was aged at 500 °C for a few hundred hours but no TiC nanoprecipitates formed. Under irradiation, TiC formed in the c.w. material at 450 °C within a few hours, only in the irradiated layer. Since only one dose was investigated, it is uncertain how quickly the phase formed, but the fact that the precipitates are enveloped by shells enriched with Ni and Si demonstrates that the MC precipitates formed prior to significant RIS development. Hence it is assumed that, at the point of observation, their dynamics and stability are independent of the compositional fluctuations brought on by RIS. Under this assumption, the enhanced nucleation of MC under irradiation can be explained by two factors: point defect supersaturation which enhances diffusion in general, and a chemical effect of a vacancy supersaturation which promotes the formation of oversized phases such as MC [63]. However, radiation can also lead to gradual re-dissolution of thermal precipitates if the cascade impacts directly on a particle, which causes constituting atoms to be ejected into the surrounding matrix. The stability of thermal precipitates under irradiation depends on a balance between these factors.

The behavior of the MC precipitates at the different irradiation temperatures can be explained on the basis of these competing factors. The Nelson-Hudson-Mazey (NHM) model [64], equation 4, expresses the balance between recoil redissolution and radiation enhanced diffusion. The model is highly simplified: it assumes a static and known number density of precipitates ρ, and it assumes that all particles have the same radius r_p. The first term expresses that the radius can shrink over time

due to a flux of atoms out of the particle by recoil: ζK_0, with the constant $\zeta \approx 10^{18}$ m^{-2}$^{-2}$ [63], K_0 the displacement rate in dpa/s, and V_{at} the atomic volume. The second term expresses the growth of the particle via diffusion towards the particle, with D the radiation enhanced diffusion coefficient of the rate limiting species in the precipitate, C the total concentration of this species in the material, and C_p the concentration of the species inside the precipitates. D can be approximated by $\approx D_v C_v V_{at}$ with D_v the diffusion coefficient of vacancies and C_v the vacancy concentration. The last term takes into consideration the growth of other MC nanoprecipitates via ρ, and hence acts as a conservation of mass term. The model predicts that given infinite time the precipitates will evolve to a steady state size that balances growth and recoil dissolution.

$$\frac{\mathrm{d}r_p}{\mathrm{d}t} = -\zeta K_0 V_{at} + \frac{3DC}{4\pi r_p C_p} - r_p^2 D\rho \tag{4}$$

The steady state size was calculated for the various irradiation conditions by setting $\mathrm{d}r_p/\mathrm{d}t = 0$ and solving for r_p. It was assumed Ti is the rate limiting species. The displacement rate K_0 used was 2.7×10^{-4} dpa/s (50 dpa/52 hours) as calculated by SRIM for the ion irradiation; the other parameters used for these calculations are given in Appendix A. Since the NHM model does not model nucleation nor predict the particle number density ρ, the steady state radius was calculated using the experimentally determined ρ given in Fig. 9. To include the irradiation at 300 °C in the model, ρ for this condition was taken to be the number density of Si clusters in table 2, since most contained a Ti cluster which might be small nuclei of TiC. An accurate estimate for ρ is not necessary at these low temperatures and even setting ρ to 0 yielded similar results, because the first two terms in equation 4 dominate. Fig. 11(a) shows the predicted steady state radius plot versus the observed average radius. Since no average radius could be experimentally determined at 300 °C, it was set to 0 for this condition. If points lie on the line $x = y$ it indicates a perfect fit between the model and experiment radii from Fig. 9. The uncertainties in the x-direction are the same uncertainties as shown in Fig. 9. The uncertainties in the y-direction result from the uncertainties in the number densities. The predicted and observed values are in quite good agreement given the simplicity of the model, given that many quantities (ζ, C_v, D, K_0, ...) are only accurate to within an order of magnitude, and given that the actual precipitate population may not yet have reached the steady state after 50 dpa. The model helps to explain why there is such a large difference between the microstructure at 300 °C and 450 °C but not between 450 °C and 600 °C. At 300 °C diffusion is slow and the first term dominates. At the higher temperatures diffusion competes and the main limitation on the size is the growth of other particles. Only very small precipitates are expected to be stable at 300 °C; the small Ti clusters observed in the APT experiments may account for these.

While the steady state size is in reasonable agreement with the observed size, the rate at which the precipitates reach this size is significantly underestimated by the model. This is illustrated in Fig. 11 (b) which shows the predicted size evolution of precipitates irradiated at 300 °C for three different dose rates: 3×10^{-4} (black), 3×10^{-3} (red) and 3×10^{-2} (blue) dpa/s. Paths are shown for starting radius 5 nm (dotted lines), a size that was occasionally observed in the MC precipitates in the aged material, as well as starting from a size close to 0 (continuous lines). The shrinkage of 5 nm particles follows a nearly linear path in the beginning as the first term in equation 4, which is a constant, dominates. The slope is determined by ζK_0. The black lines show the expected paths for a dose rate close to the estimated dose rate in the region of material that was studied. After 50 dpa, large MC precipitates are not expected to have shrunk appreciably. However, experimentally, no MC precipitates were found any longer in the irradiated layer of the aged material. This suggests that ζ is strongly underestimated. A higher
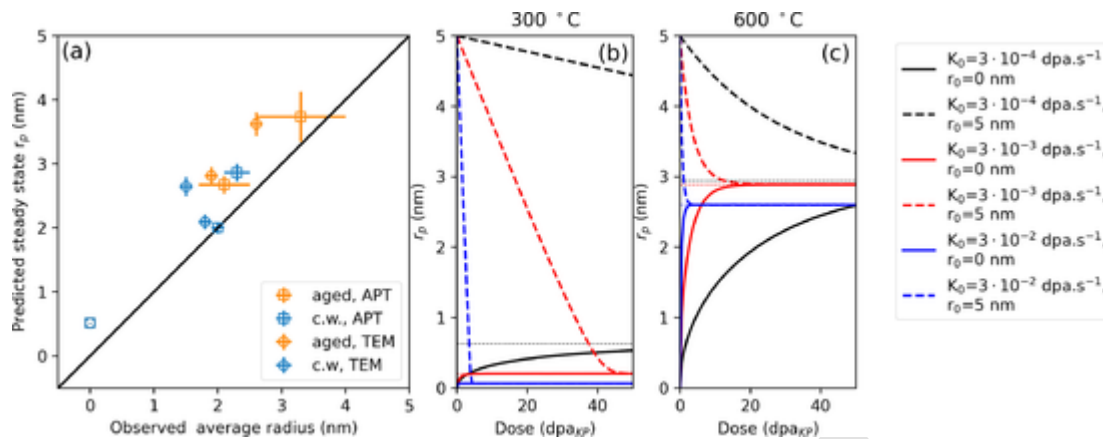
Fig. 11. (a) The predicted steady-state radius of TiC precipitates, calculated using the NHM model [64] and the experimentally determined number density, plotted versus the observed average radius. (b) Average particle radius evolution for irradiation at 300 ℃ at different dose rates and starting sizes as predicted by the NHM model. (c) Average particle radius evolution for irradiation at 600 ℃ at different dose rates and starting sizes as predicted by the NHM model. The legend on the right pertains to both (b) and (c).

ζ would also bring the points in Fig. 11 (a) closer to the $x = y$ line. The same calculations were performed for 600 ℃; they are shown in Fig. 11 (c). A precipitate number density of $\rho = 4 \times 10^{22}$ m^{-3} was used for the calculation. Due to increased diffusion, the model predicts the system will evolve to steady state faster than at 300 ℃. The opposite was observed in the experiment, with the 600 ℃/aged condition still showing remnants from the original precipitate population. A possible explanation is that the NHM model does not account for concentration gradients in the matrix, particularly in the vicinity around the precipitates. The atoms ejected from the precipitates due to recoil tend to remain near the precipitate. At higher temperatures with increased diffusion rates, these atoms are more likely to diffuse back to the same precipitate than away to the bulk, effectively stabilizing the precipitates.

Despite dose rate spanning 3 orders of magnitude in Fig.s 11 (b) and (c), the predicted steady state sizes are within about 0.5 nm from each other both for 300 and 600 ℃. This demonstrates that, if the precipitate populations are assumed to be close to the steady state at 50 dpa, no observable gradients in precipitate size are expected over the extent of the irradiated layer. This would again suggest the feature observed in the 450 ℃/aged condition (Fig. 8) is an artifact.

The differences in number density of MC precipitates between the c.w. and aged materials can not be explained on the basis of the NHM model. The predicted growth kinetics are very different from those observed and the model does not predict nucleation. The differences between the c.w. and aged material can instead be rationalized on the basis of classical nucleation arguments. In the c.w. material, the Ti concentration in solid solution is about 3 times higher compared to the aged material. Hence, when radiation at elevated temperatures increases the point defect supersaturation and rates of diffusion, nucleation of new precipitates is enhanced much more in the c.w. material than in the aged material. In the aged material, the number density of the pre-irradiation population of TiC nanoprecipitates is smaller than the number density that could form under irradiation; there are far more excess vacancies under irradiation which promotes nucleation. In addition, ageing occured at a higher temperature than the irradiation temperature; higher temperatures tend to favor growth over nucleation. The NHM model shows that recoil redissolution tends to be slow, so the thermally formed MC precipitates are slow to shrink compared to the formation rate of new TiC under irradiation. This means that the Ti concentration remains lower in the aged materials for an extended period of time. As long as it remains low, the probability of forming a critical Ti cluster which nucleates as MC is decreased. If it were not for other processes, the aged and c.w. microstructures should converge after a long enough irradiation time. However, RIS happens on a similar timescale as redissolution, and Ti is also found in G-phase. Likely, the lower Ti concentration in solid solution leads to the increased probability that Ti is swept away by RIS before critical MC clusters can form, and is instead incorporated into G-phase. Hence, the population of thermally formed precipitates acts as a barrier to achieve the full MC precipitation potential, and the final number density is reduced as a result. The lower number density of MC precipitates results in higher RIS gradients which promotes G-phase. This explains the differences in the microstructures of Fig. 10 (e) and (f).

The actual service conditions for this material will be very different from those applied in the ion irradiation of this study. Predicting the behavior under those conditions requires extrapolating the MC stability domain, which is not straightforward. The structural materials inside a reactor core typically experience damage rates between 10^{-8}–10^{-6} dpa/s, two to four orders of magnitude lower than during ion irradiation. Since recoil resolution is reduced, the NHM model predicts that the steady-state precipitate size is larger at lower dose rates for the same irradiation temperature. Consequently, the precipitates should also form and be stable at lower temperatures. Using the stability criterion of Abromeit et al. [65], the precipitates are expected to be stable at a temperature approximately 50 ℃ lower than the lower limit under ion irradiation relevant dose rates. Additional figures related to these calculations are given in the supplementary materials. Both these models neglect the chemical effect of vacancies on nucleation. Since TiC has a larger lattice parameter than austenite, its nucleation is enhanced by the vacancy supersaturation induced by irradiation [63,66]. At lower dose rates, the vacancy supersaturation decreases significantly, which may in turn reduce nucleation and stability of the precipitates. This could partly explain why earlier reports [36,67] concluded TiC is unstable below 550 ℃ under neutron irradiation; they found that the precipitates were absent in both initially cold worked and aged material after short irradiations. On the other hand, TiC formation was also reported in a very similar material after neutron irradiation at 300 ℃ [14]. Additional experiments at lower dose rates may help clarify the competing effects of increased stability due to decreased recoil resolution and decreased stability due to reduced vacancy supersaturation.

5. Conclusion

In this work, Ti stabilized steels in a c.w. and aged condition were irradiated with Fe ions to investigate the behavior of Ti and TiC precipitates under irradiation. By studying the microstructure at the nano scale with TEM and APT, an improved understanding was obtained of the interactions between the TiC nanoprecipitates, other alloying elements, and the formation of radiation induced precipitates.

- TiC nanoprecipitates redissolved or did not form under Fe-ion irradiation at 300 °C. After irradiation at 450 °C and 600 °C nanoprecipitates were found in both the aged and c.w. materials. This behavior was explained in semi-quantitative terms using the NHM model. The model predicts that the precipitates will be more stable in a real reactor environment due to the lower dose rates, but this must be verified.
- At all irradiation temperatures, Si, Ni, P and Ti formed clusters. At 300 °C, Ti forms clusters through a mechanism other than RIS. At higher irradiation temperatures, Ti always co-segregated with Si and Ni, indicative of RIS.
- G-phase was identified at elevated irradiation temperatures by the enrichment of Mn in APT measurements, and from the combination of diffraction patterns and DF images. G-phase was also enriched in Ti, and precipitates were often attached to TiC nanoprecipitates.
- Ageing resulted in a lower TiC nanoprecipitate number density and a higher G-phase volume fraction after irradiation. This suggests TiC precipitates are important point defect sinks that delay radiation induced microstructural instability, hence their number density should be maximized in order to optimize the material. This is best achieved by maximizing the Ti supersaturation and ensuring the element is homogeneously distributed as is the case in the c.w. material. Ageing is counterproductive to achieving the full nucleation potential.

Declaration of Competing Interest

The authors declare that they have no known competing financial interests or personal relationships that could have appeared to influence the work reported in this paper.

Acknowledgements

Appendix A. NHM model parameters

For the NHM model calculations, Ti was assumed to be the critical element to precipitate formation. In equation 4, the total concentration of Ti (C) and the concentration of Ti in the precipitates (C_p) were taken to be 0.3 at% and 40 at% respectively (see section 2).

As stated in the text, the radiation enhanced diffusion coefficient of Ti was calculated with $D = D_v C_v V_{at}$ with $V_{at} \approx 1.2 \times 10^{-29}$ m^3. The diffusion coefficients of point defects (vacancies: D_v, self-interstitials: D_i) were calculated with expression from [68] and given in Eq. A.1a and A.1b.

$$D_v \left(\text{m}^2/\text{s} \right) = 6 \times 10^{-5} \exp \left(\frac{-15666}{T(\text{K})} \right) \tag{A.1a}$$

$$D_i \left(\text{m}^2/\text{s} \right) = 1 \times 10^{-7} \exp \left(\frac{-4990}{T(\text{K})} \right) \tag{A.1b}$$

The vacancy concentration C_v was calculated by solving for the steady-state in the static rate equations [57]; the solution is given in

Eq. A.2.

$$C_v \left(\text{m}^{-3} \right) = \frac{-K_{s,i}}{2K_{i,v}} + \frac{1}{2} \sqrt{ \left(\frac{K_{s,i}}{K_{i,v}} \right)^2 + \frac{4K_0 \varepsilon K_{s,i}}{V_{at} K_{i,v} K_{s,v}} } \tag{A.2}$$

The cascade efficiency ε was assumed to be 3% [56]. In the equation, $K_{s,i}$, $K_{s,v}$ and $K_{i,v}$ are the rate constants with which interstitials annihilate at sinks, vacancies annihilate at sinks, and interstitials recombine with vacancies respectively. It was assumed that for the point defect balances the only important sinks were dislocations, which yields expressions A.3a, A.3b and A.3c. The bias factors z_i and z_v were taken from [68] and set to 1.1 and 1 respectively. A typical steady state dislocation density under irradiation of $\rho_l = 6 \times 10^{14}$ m^{-2} was assumed [54]. The vacancy-interstitial interaction distance r_{iv} was set to 7×10^{-10} m [68].

$$K_{s,i} \left(\text{s}^{-1} \right) = z_i \rho_l D_i \tag{A.3a}$$

$$K_{s,v} \left(\text{s}^{-1} \right) = z_v \rho_l D_v \tag{A.3b}$$

$$K_{i,v} \left(\text{m}^3 \text{s}^{-1} \right) = 4\pi \left(D_v + D_i \right) r_{iv} \tag{A.3c}$$

Supplementary material

Supplementary material associated with this article can be found, in the online version, at 10.1016/j.actamat.2020.07.022

References

[1] H Abderrahim, P Baeten, D De Bruyn, J Heyse, P Schuurmans, J Wagemans, MYRRHA : a multipurpose hybride research reactor for high-end applications, Nucl. Phys. News 20 (1) (2010) 24–28, doi:10.1080/10506890903178913.
[2] J Séran, M Le Flem, Irradiation-Resistant Austenitic Steels as Core Materials for Generation IV Nuclear Reactors, in: P Yvon (Ed.), Struct. Mater. Gener. IV Nucl. React., 1st ed., Woodhead Publishing, Cambridge, 2017, pp. 285–328.
[3] C Cawthorne, E J Fulton, Voids in irradiated stainless steel, Nature 216 (5115) (1967) 575–576, doi:10.1038/216575a0.
[4] K Russell, The theory of void nucleation in metals, Acta Metall. 26 (10) (1978) 1615–1630, doi:10.1016/0001-6160(78)90071-8.
[5] W Wolfer, Fundamental Properties of Defects in Metals, in: R Konings (Ed.), Compr. Nucl. Mater., 1, Elsevier, Amsterdam, New York, 2012, pp. 1–45.
[6] D C Crawford, D L Porter, S L Hayes, Fuels for sodium-Cooled fast reactors: US perspective, J. Nucl. Mater. 371 (1–3) (2007) 202–231, doi:10.1016/j.jnucmat.2007.05.010.
[7] J Seran, V Levy, P Dubuisson, D Gilbon, A Maillard, A Fissolo, H Touron, R Cauvin, A Chalony, E Leboulin, E Le Boulbin, E Leboulbin, Behavior under Neutron-Irradiation of the 15-15Ti and EM10 Steels Used as Standard Materials of the PHENIX Fuel Subassembly, in: R E Stoller, A S Kumar, D S Gelles (Eds.), Eff. Radiat. Mater. 15th Int. Symp., 1125, ASTM publication, Nashville, USA, 1992, pp. 1209–1233.
[8] P Dubuisson, A Maillard, C Delalande, D Gilbon, J Seran, The Effect of Phosphorus on the Radiation-Induced Microstructure of Stabilized Austenitic Stainless Steels, in: R E Stoller, A S Kumar, D S Gelles (Eds.), Eff. Radiat. Mater. 15th Int. Symp., 1125, ASTM publication, Nashville, USA, 1992, pp. 995–1014.
[9] J Seran, H Touron, A Maillard, P Dubuisson, J Hugot, E Le Boulbin, P Blanchard, M Pelletier, The Swelling Behavior of Titanium Stabilized Austenitic Steels Used as Structural Materials of Fissile Subassemblies in Phenix, Eff. Radiat. Mater. 14th Int. Symp., 2, ASTM publication, Andover, USA, 1990, pp. 739–752.
[10] S I Porollo, Y V Konobeev, F A Garner, Swelling and microstructure of austenitic stainless steel ChS-68 CW after high dose neutron irradiation, J. Nucl. Mater. 393 (1) (2009) 61–66.
[11] I Neklyudov, V Voyevodin, Radiation swelling of modified austenitic steels, Russ. Phys. J. 51 (4) (2008) 400–413, doi:10.1007/s11182-008-9063-9.
[12] R Hasiguti, Japanese program of materials research for fusion reactors, J. Nucl. Mater. 103 (0) (1981) 51–55, doi:10.1016/0022-3115(82)90573-6.
[13] I Shibahara, N Akasaka, S Onose, H Okada, S Ukai, Swelling of advanced austenitic stainless-Steels developed for the environment of heavy neutron exposure, J. Nucl. Mater. 212 (1994) 487–491, doi:10.1016/0022-3115(94)90109-0.
[14] M Suzuki, S Hamada, P Maziasz, S Jitsukawa, A Hishinuma, Compositional behavior and stability of MC-type precipitates in JPCA austenitic stainless steel during HFIR irradiation, J. Nucl. Mater. 191–194 (PART B) (1992) 1351–1355, doi:10.1016/0022-3115(92)90695-H.
[15] T Jayakumar, M Mathew, K Laha, R Sandhya, Materials development for fast reactor applications, Nucl. Eng. Des. 265 (0) (2013) 1175–1180, doi:10.1016/j.nucengdes.2013.05.001.

[16] F Garner, Recent insights on the swelling and creep of irradiated austenitic alloys, J. Nucl. Mater. 122 (1–3) (1984) 459–471, doi:10.1016/0022-3115(84)90641-x.

[17] R Hübner, K Ehrlich, Influence of Minor Alloy Elements on Irradiation-induced Thresholds of Austenitic Steel DIN 1.4970 at High Neutron Doses, Annu. Meet. Nucl. Technol. '98, Proc., 1998, pp. 737–740.

[18] P Maziasz, Void swelling resistance of phosphorus-modified austenitic stainless steels during HFIR irradiation at 300–500 ×c to 57 dpa, J. Nucl. Mat. 200 (1) (1993) 90–107, doi:10.1016/0022-3115(93)90013-O.

[19] P Maziasz, Overview of microstructural evolution in neutron-Irradiated austenitic stainless steels, J. Nucl. Mater. 205 (C) (1993) 118–145, doi:10.1016/0022-3115(93)90077-C.

[20] F Garner, H Brager, The influence of Mo, Si, P, C, Ti, Cr, Zr and various trace-Elements on the neutron-Induced swelling of AISI-316 stainless-Steel, J. Nucl. Mater. 155 (1988) 833–837, doi:10.1016/0022-3115(88)90425-4.

[21] K Herschbach, W Schneider, K Ehrlich, Effects of minor alloying elements upon swelling and in-pile creep in model plain fe-15cr-15ni stainless steels and in commercial DIN 1.4970 alloys, J. Nucl. Mat. 203 (203) (1993) 233–248.

[22] P Yvon, M Le Flem, C Cabet, J Seran, Structural materials for next generation nuclear systems: challenges and the path forward, Nucl. Eng. Des. 294 (2015) 161–169, doi:10.1016/j.nucengdes.2015.09.015.

[23] W Kesternich, Dislocation-Controlled precipitation of TiC particles and their resistance to coarsening, Philos. Mag. A 52 (4) (1985) 533–548, doi:10.1080/01418618508237645.

[24] P Maziasz, C McHargue, Microstructural evolution in annealed austenitic steels during neutron irradiation, Int. Mater. Rev. 32 (1) (1987) 190–219, doi:10.1179/095066087790150331.

[25] P Maziasz, Swelling and swelling resistance possibilities of austenitic stainless steels in fusion reactors, J. Nucl. Mater. 122 (13) (1984) 472–486, doi:10.1016/0022-3115(84)90642-1.

[26] E Lee, L Mansur, Relationships between phase stability and void swelling in fe-Cr-Ni alloys during irradiation, Metall. Trans. A 23 (7) (1992) 1977–1986, doi:10.1007/BF02647545.

[27] Z Jiao, G Was, Novel features of radiation-Induced segregation and radiation-Induced precipitation in austenitic stainless steels, Acta Mater. 59 (3) (2011) 1220–1238, doi:10.1016/J.ACTAMAT.2010.10.055.

[28] H Jin, E Ko, S Lim, J Kwon, C Shin, Effect of irradiation temperature on microstructural changes in self-Ion irradiated austenitic stainless steel, J. Nucl. Mater. 493 (2017) 239–245, doi:10.1016/j.jnucmat.2017.06.019.

[29] A Etienne, B Radiguet, N Cunningham, G Odette, P Pareige, Atomic scale investigation of radiation-Induced segregation in austenitic stainless steels, J. Nucl. Mater. 406 (2) (2010) 244–250, doi:10.1016/J.JNUCMAT.2010.08.043.

[30] S Bruemmer, E Simonen, P Scott, P Andresen, G Was, J Nelson, Radiation-Induced material changes and susceptibility to intergranular failure of light-Water-Reactor core internals, J. Nucl. Mater. 274 (3) (1999) 299–314, doi:10.1016/S0022-3115(99)00075-6.

[31] E Kenik, K Hojou, Radiation-Induced segregation in FFTF-Irradiated austenitic stainless steels, J. Nucl. Mater. 191–194 (1992) 1331–1335, doi:10.1016/0022-3115(92)90691-D.

[32] P J Maziasz, Formation and stability of radiation-Induced phases in neutron-Irradiated austenitic and ferritic steels, J. Nucl. Mater. 169 (C) (1989) 95–115, doi:10.1016/0022-3115(89)90525-4.

[33] A Etienne, B Radiguet, P Pareige, Understanding silicon-Rich phase precipitation under irradiation in austenitic stainless steels, J. Nucl. Mater. 406 (2) (2010) 251–256, doi:10.1016/j.jnucmat.2010.08.045.

[34] Z Jiao, G Was, Precipitate behavior in self-Ion irradiated stainless steels at high doses, J. Nucl. Mater. 449 (1–3) (2014) 200–206, doi:10.1016/j.jnucmat.2014.02.026.

[35] A Rowcliffe, E Lee, The Stability of the MC Phase in a Stainless Steel Irradiated in Various Environments, Dimens. Stab. Mech. Behav. Irradiat. Met. Alloy., Thomas Telford Publishing, 1984, pp. 5–9.

[36] K Ehrlich, Auswirkungen von Ausscheidungen auf das Bestrahlungsinduzierte Schwellverhalten und die Hochtemperaturversprödung in dem Austenitischen stahl X10 crnimotib 15 15, Z. Met. 94 (94) (2003) 5.

[37] J S Zhang, N Li, Review of the studies on fundamental issues in LBE corrosion, J. Nucl. Mater. 373 (1–3) (2008) 351–377, doi:10.1016/j.jnucmat.2007.06.019.

[38] R Delville, E Stergar, M Verwerft, Results of a New Production of Nuclear-Grade 1.4970 15-15Ti Stainless Steel Fuel Cladding Tubes for GEN IV Reactors, 22nd Int. Conf. Nucl. Eng. ICONE22, ASME, Prague, Czech Republic, 2014.

[39] ASTM International, ASTM E1019-11, Standard Test Methods for Determination of Carbon, Sulfur, Nitrogen, and Oxygen in Steel, Iron, Nickel, and Cobalt Alloys by Various Combustion and Fusion Techniques, 2011.

[40] N Cautaerts, R Delville, E Stergar, D Schryvers, M Verwerft, Tailoring the Ti-C nanoprecipitate population and microstructure of titanium stabilized austenitic steels, J. Nucl. Mater. 507 (2018) 177–187, doi:10.1016/j.jnucmat.2018.04.041.

[41] N Cautaerts, R Delville, E Stergar, D Schryvers, M Verwerft, Characterization of (Ti,Mo,Cr)C nanoprecipitates in an austenitic stainless steel on the atomic scale, Acta Mater. 164 (2018) 90–98, doi:10.1016/J.ACTAMAT.2018.10.018.

[42] J Ziegler, M Ziegler, J Biersack, SRIM - The Stopping and range of ions in matter (2010), Nucl. Instruments Methods Phys. Res. Sect. B Beam Interact. with Mater. Atoms 268 (11–12) (2010) 1818–1823, doi:10.1016/j.nimb.2010.02.091.

[43] R Stoller, M Toloczko, G Was, A Certain, S Dwaraknath, F Garner, On the use of SRIM for computing radiation damage exposure, Nucl. Instruments Methods

[44] Phys. Res. Sect. B Beam Interact. with Mater. Atoms 310 (2013) 75–80, doi:10.1016/j.nimb.2013.05.008.

[44] G Kinchin, R Pease, The displacement of atoms in solids, Reports Prog. Phys. 18 (1955) 1–51, doi:10.1088/0034-4885/18/1/301.

[45] D. Haley, A. Ceguerra, 3Depict - Visualisation & Analysis for Atom Probe, 2015.

[46] E Lee, P Maziasz, A Rowcliffe, The Structure and Composition of Phases Occurring in Austenitic Stainless Steels in Thermal and Irradiation Environments, Technical Report, Oak Ridge National Lab., 1980.

[47] M Thuvander, J Weidow, J Angseryd, L Falk, F Liu, M Sonestedt, K Stiller, H Andrén, Quantitative atom probe analysis of carbides, Ultramicroscopy 111 (6) (2011) 604–608, doi:10.1016/j.ultramic.2010.12.024.

[48] I Shuro, H Kuo, T Sasaki, K Hono, Y Todaka, M Umemoto, G-Phase precipitation in austenitic stainless steel deformed by high pressure torsion, Mater. Sci. Eng. A 552 (2012) 194–198, doi:10.1016/j.msea.2012.05.030.

[49] Z Jiao, S Bruemmer, D Edwards, Others, Aging and Embrittlement of High Fluence Stainless Steels, Technical Report, Battelle Energy Alliance, LLC, 2012.

[50] A Renault-Laborne, J Malaplate, C Pokor, B Tanguy, Characterization of precipitates in 316 stainless steel neutron-Irradiated at 390 ×c by the combination of CDF-TEM, EF-TEM, and HR-TEM, Eff. Radiat. Nucl. Mater. (2014) 1–24, doi:10.1520/stp157220130096.

[51] T Malis, S C Cheng, R F Egerton, EELS Log-Ratio technique for specimen-Thickness measurement in the TEM, J. Electron Microsc. Tech. 8 (1988) 193–200, doi:10.1002/jemt.1060080206.

[52] K Iakoubovskii, K Mitsuishi, Y Nakayama, K Furuya, Thickness measurements with electron energy loss spectroscopy, Microsc. Res. Tech. 71 (8) (2008) 626–631, doi:10.1002/jemt.20597.

[53] R Egerton, Electron energy-Loss spectroscopy in the electron microscope, 3rd ed., Springer, New York, 2011, doi:10.1007/978-1-4419-9583-4.

[54] S Zinkle, L Seitzman, W Wolfer, Stability of vacancy clusters in metals: energy calculations for pure metals, Philos. Mag. A 55 (1) (1987) 111–125, doi:10.1080/01418618708209803.

[55] G Was, J Wharry, B Frisbie, B Wirth, D Morgan, J Tucker, T Allen, Assessment of radiation-Induced segregation mechanisms in austenitic and ferritic-Martensitic alloys, J. Nucl. Mater. 411 (1–3) (2011) 41–50, doi:10.1016/j.jnucmat.2011.01.031.

[56] G Was, T Allen, Radiation-Induced segregation in multicomponent alloys: effect of particle type, Mater. Charact. 32 (4) (1994) 239–255, doi:10.1016/1044-5803(94)90101-5.

[57] G Was, Fundamentals of radiation materials science, 2nd ed., Springer, New York, 2017, doi:10.1007/978-1-4939-3438-6.

[58] E Lee, L Mansur, Fe-15ni-13cr austenitic stainless steels for fission and fusion reactor applications. II. effects of minor elements on precipitate phase stability during thermal aging, J. Nucl. Mater. 278 (1) (2000) 20–29, doi:10.1016/S0022-3115(99)00236-6.

[59] T Allen, J Cole, J Gan, G Was, R Dropek, E Kenik, Swelling and radiation-Induced segregation in austentic alloys, J. Nucl. Mater. 342 (1–3) (2005) 90–100, doi:10.1016/j.jnucmat.2005.02.008.

[60] A Rowcliffe, E Lee, High temperature radiation damage phenomena in complex alloys, J. Nucl. Mater. 108–109 (C) (1982) 306–318, doi:10.1016/0022-3115(82)90500-1.

[61] K Farrell, Experimental effects of helium on cavity formation during irradiationa review, Radiat. Eff. 53 (3–4) (1980) 175–194, doi:10.1080/00337578008207114.

[62] A Padilha, G Schanz, K Anderko, Ausscheidungsverhalten des titanstabilisierten austenitischen stahls 15% cr-15% ni-1% mo-Ti-B (DIN-werkstoff-nr. 1.4970), J. Nucl. Mater. 105 (1) (1982) 77–92, doi:10.1016/0022-3115(82)90454-8.

[63] K Russell, Phase stability under irradiation, Prog. Mater. Sci. 28 (3–4) (1984) 229–434, doi:10.1016/0079-6425(84)90001-X.

[64] R Nelson, J Hudson, D Mazey, The stability of precipitates in an irradiation environment, J. Nucl. Mater. 44 (3) (1972) 318–330, doi:10.1016/0022-3115(72)90043-8.

[65] C Abromeit, V Naundorf, H Wollenberger, Phase stability criteria for ion and neutron irradiated alloys, J. Nucl. Mater. 155–157 (1988) 1174–1178, doi:10.1016/0022-3115(88)90491-6.

[66] M Mruzik, K Russell, The effect of irradiation on the nucleation of incoherent precipitates, J. Nucl. Mater. 78 (2) (1978) 343–353, doi:10.1016/0022-3115(78)90456-7.

[67] H Bergmann, W Dietz, K Ehrlich, G Muhling, M Schirra, Entwicklung des Werkstoffs X10CrNiMoTiB 15 15 als Strukturmaterial für Brennelemente, Technical Report, Forschungszentrum Karlsruhe, 2003.

[68] C Pokor, Y Brechet, P Dubuisson, J Massoud, A Barbu, Irradiation damage in 304 and 316 stainless steels: experimental investigation and modeling. part I: evolution of the microstructure, J. Nucl. Mater. 326 (1) (2004) 19–29, doi:10.1016/J.JNUCMAT.2003.11.007.